Differential porosimetry and permeametry for random porous media

R. Hilfer and A. Lemmer
ICP, Universität Stuttgart, Allmandring 3, 70569 Stuttgart Germany
(Received 5 January 2015; published 7 July 2015)

Accurate determination of geometrical and physical properties of natural porous materials is notoriously difficult. Continuum multiscale modeling has provided carefully calibrated realistic microstructure models of reservoir rocks with floating point accuracy. Previous measurements using synthetic microcomputed tomography (μ-CT) were based on extrapolation of resolution-dependent properties for discrete digitized approximations of the continuum microstructure. This paper reports continuum measurements of volume and specific surface with full floating point precision. It also corrects an incomplete description of rotations in earlier publications. More importantly, the methods of differential permeametry and differential porosimetry are introduced as precision tools. The continuum microstructure chosen to exemplify the methods is a homogeneous, carefully calibrated and characterized model for Fontainebleau sandstone. The sample has been publicly available since 2010 on the worldwide web as a benchmark for methodical studies of correlated random media. High-precision porosimetry gives the volume and internal surface area of the sample with floating point accuracy. Continuum results with floating point precision are compared to discrete approximations. Differential porosities and differential surface area densities allow geometrical fluctuations to be discriminated from discretization effects and numerical noise. Differential porosimetry and Fourier analysis reveal subtle periodic correlations. The findings uncover small oscillatory correlations with a period of roughly 850 μm, thus implying that the sample is not strictly stationary. The correlations are attributed to the deposition algorithm that was used to ensure the grain overlap constraint. Differential permeabilities are introduced and studied. Differential porosities and permeabilities provide scale-dependent information on geometry fluctuations, thereby allowing quantitative error estimates.

DOI: 10.1103/PhysRevE.92.013305 PACS number(s): 46.15.−x, 81.05.Rm, 78.55.Mb, 61.43.Gt

I. INTRODUCTION

Accurate determination of geometrical or physical properties of natural porous materials requires accurate geometrical microstructure as emphasized by numerous authors [1–5]. Digital images obtained from microcomputed tomography (μ-CT) provide only a rough approximation of the microstructure with a resolution typically in the μm range which is often insufficient for multiscale media and multiscale methods [6–9].

Modeling of realistic random media has recently received increasing attention in mathematics and physics of complex materials and porous media [10–20]. An accurate, calibrated and well-characterized reference structure of porous Fontainebleau sandstone was provided in [21,22]. It can be used for testing and benchmarking analytical and numerical methods in a realistic medium. Our objective in this paper is to develop an algorithm to compute porosity and surface area density with floating point precision. Realizing that extrapolation of discrete approximations is insufficient [22], one is forced to consider direct analysis of continuum data. Experimentally, Fontainebleau sandstone has been and still is frequently used as an example for a realistic, yet simple, example of a porous consolidated geomaterial [23–28]. Many investigations consider Fontainebleau sandstone, because it is a rare example of a simple natural porous medium with intergranular porosity varying from about 0.02 to 0.28 without large change in grain granulometry.

Differential porosimetry and differential permeametry refer to the quantitative analysis of their derivatives with respect to volume. Examples are porosity, internal surface area, or permeability. In both methods it is necessary to prepare samples that differ only infinitesimally and to compute the observables with sufficiently high precision, so that their derivatives remain unaffected by numerical noise.

Given the set $\mathbb{P} \subset \mathbb{R}^3$ (pore space), assumed to be the realization of a random medium inside a region $\mathbb{S} \subset \mathbb{R}^3$ (sample region), its permeability $k(\mathbb{P})$ is obtained [4] from (spatially averaging) the velocity field $\mathbf{v}(\mathbf{x})$ that solves the dimensionless boundary value problem

$$\Delta \mathbf{v}(\mathbf{x}) = \nabla p(\mathbf{x}), \quad \mathbf{x} \in \mathbb{P} \cap \mathbb{S}, \tag{1a}$$

$$\nabla \cdot \mathbf{v}(\mathbf{x}) = 0, \quad \mathbf{x} \in \mathbb{P} \cap \mathbb{S}, \tag{1b}$$

$$p(\mathbf{x}) = 0, \quad \mathbf{x} \in \mathbb{P} \cap \partial\mathbb{S}_{\mathrm{o}}, \tag{1c}$$

$$p(\mathbf{x}) = 1, \quad \mathbf{x} \in \mathbb{P} \cap \partial\mathbb{S}_{\mathrm{i}}, \tag{1d}$$

$$\mathbf{v}(\mathbf{x}) = \mathbf{0}, \quad \mathbf{x} \in \partial(\mathbb{P} \cap \mathbb{S}) \setminus (\partial\mathbb{S}_{\mathrm{i}} \cup \partial\mathbb{S}_{\mathrm{o}}) \tag{1e}$$

for stationary laminar fluid flow in the domain $\mathbb{P}$, where Δ is the Laplacian, $p(\mathbf{x})$ denotes the pressure field, $\partial\mathbb{P}$ is the boundary of $\mathbb{P}$, $\partial\mathbb{S}$ is the sample boundary, $\partial\mathbb{S}_{\mathrm{i}} \subset \partial\mathbb{S}$ is the inlet boundary, and $\partial\mathbb{S}_{\mathrm{o}} \subset \partial\mathbb{S}$ is the outlet. Laminar fluid flow within a random pore space $\mathbb{P}$ occurs in numerous applied problems ranging from hydrology to petroleum engineering (see [4] and references therein). One would like to predict the dependence of the permeability $k(\mathbb{P})$ on the random geometry $\mathbb{P}$ without detailed knowledge of $\mathbb{P}$. Randomness and lack of exact knowledge of $\mathbb{P}$ suggest employing averaged geometric quantities such as porosity $\phi(\mathbb{P})$, defined in (9), or internal surface area density $\sigma(\mathbb{P})$, defined in Eq. (10), and assuming that a functional relation such as

$$k(\mathbb{P}) \approx k(\phi(\mathbb{P}), \sigma(\mathbb{P}), \dots) \tag{2}$$

holds with high probability for the microstructures of interest [4,29–32]. Investigating the existence or nonexistence of a functional relation such as Eq. (2) becomes possible if its geometric and physical quantities can be computed with high precision. Already the computation of precise *volumina*

or porosities for random geometries, however, has to our knowledge never been accomplished and remains currently limited to extrapolation from discrete approximations [22]. More difficult, and still an unsolved problem at present, is the computation of floating point precise permeabilities $k(\mathbb{P})$ for the continuum model.

II. PROBLEM AND OBJECTIVE

The objective of this paper is to compute geometric properties of the continuum microstructure of Fontainebleau sandstone [21] with floating point precision. The aim of such analysis is threefold. First, it is a prerequisite for precise tests and understanding of the relation between geometric and physical quantities. Second, high numerical precision is needed to distinguish geometric fluctuations and correlations from numerical noise or discretization artefacts. Third, high precision allows a quantitative test of the pervasive but elusive concept of representative elementary volumes (REVs) for homogeneous media.

The computation of precise physical or geometrical properties for a random three-dimensional continuum microstructure is difficult. To the best of our knowledge all computations for sedimentary rocks (such as sandstones or limestones) are at present restricted to experimental or synthetic μ-CT approximations. The present paper reports the first computationally efficient techniques for computing floating-point-precisely volume and surface area for continuum microstructures. The technique is applied to a direct comparison between the continuum microstructure and its synthetic μ-CT images [21,22]. Differential porosities and differential permeabilities are introduced. The results are used to estimate the permeabilities and compare them with solutions of Eq. (1) for discretized approximations (synthetic μ-CT's).

III. COMPLEX MICROSTRUCTURES AS RANDOM SETS

Correlated random media, such as the Fontainebleau model of [21], may be approached computationally and mathematically as closed and random sets $\mathbb{X}$ in $\mathbb{R}^3$ [33]. For convenience of the reader its definition is recalled here. A random closed set $\mathbb{X}$ is a measurable function

$$\mathbb{X} : (\Omega,\mathcal{O},\mu) \to (\mathcal{F},\mathcal{B}(\mathcal{F})) \tag{3}$$

from a probability space $(\Omega,\mathcal{O},\mu)$ to the measurable space $(\mathcal{F},\mathcal{B}(\mathcal{F}))$ [33]. Here Ω denotes the set of outcomes or realizations, $\mathcal{O}$ the σ algebra of events, and μ the probability measure. The symbol $\mathcal{F}$ denotes the set of all closed subsets of $\mathbb{R}^3$ and its Borel σ algebra $\mathcal{B}(\mathcal{F})$ is defined as the σ algebra generated by the set system $\{\mathcal{F}^{\mathbb{K}} : \mathbb{K} \in \mathcal{C}\}$ with

$$\mathcal{F}^{\mathbb{K}} = \{\mathbb{F} \in \mathcal{F} : \mathbb{F} \cap \mathbb{K} = \emptyset\}, \tag{4}$$

where $\mathcal{C}$ is the system of all compact subsets of $\mathbb{R}^3$. The image measure $\mu_{\mathbb{X}} = \mathbb{X}(\mu)$ of μ under the map $\mathbb{X}$ is the distribution of the random closed set. For an event $A \in \mathcal{B}(\mathcal{F})$ the notation $\mu(\mathbb{X} \in A)$ stands for the probability $\mu(\{\omega \in \Omega : \mathbb{X}(\omega) \in A\})$ that $\mathbb{X} \in A$ holds. If $\mu(\mathbb{X} \in A) = 1$ then $\mathbb{X} \in A$ holds almost surely. For real-valued functions $f : \mathcal{F} \to \mathbb{R}$ the expectation value is defined as

$$\langle f(\mathbb{X})\rangle = \int_{\mathcal{F}} f(\mathbb{F}) d\mu_{\mathbb{X}}(\mathbb{F}) = \int_{\Omega} f(\mathbb{X}(\omega)) d\mu(\omega). \tag{5}$$

Two random closed sets $\mathbb{X}$ and $\mathbb{X}'$ are stochastically equivalent, written $\mathbb{X} \sim \mathbb{X}'$, if their distributions are the same, i.e., if $\mu_{\mathbb{X}} = \mu_{\mathbb{X}'}$.

A random closed set $\mathbb{X}$ is called stationary (or homogeneous) if $\mathbb{X} + \mathbf{x} \sim \mathbb{X}$ for all $\mathbf{x} \in \mathbb{R}^3$, where the notation $\mathbb{F} + \mathbf{x}$ for a set $\mathbb{F} \subset \mathbb{R}^3$ means $\mathbb{F} + \mathbf{x} = \{\mathbf{a} + \mathbf{x} : \mathbf{a} \in \mathbb{F}\}$. A random closed set $\mathbb{X}$ is called isotropic if $\mathsf{B}\mathbb{X} \sim \mathbb{X}$ for all rotations $\mathsf{B} \in \mathrm{SO}(3)$, where $\mathsf{B}\mathbb{F} := \{\mathsf{B}\mathbf{a} : \mathbf{a} \in \mathbb{F}\}$.

A nonempty stationary random closed set is almost surely unbounded [33]. This seems to exclude applications because experimental samples are always bounded. However, a bounded real-world sample may be viewed as the realization of a stationary random closed set observed in a sample region [33]. To see this let

$$\mathbb{E} = \{\mathbf{x} = (x,y,z) \in \mathbb{R}^3 : 0 \leqslant x,y,z \leqslant 1\} \tag{6}$$

denote the unit cube and let $\mathbb{X}' \subset \mathbb{E}$ denote a (random or deterministic) compact set contained in $\mathbb{E}$. Define $\mathbb{X}'' := \bigcup_{\mathbf{z}\in\mathbb{Z}^3} \mathbb{X}' + \mathbf{z}$ and let ξ be a random vector, independent of $\mathbb{X}'$, which is uniformly distributed in $\mathbb{E}$, i.e., its distribution is the Lebesgue measure restricted to $\mathbb{E}$. Then $\mathbb{X} = \mathbb{X}'' + \xi$ is a stationary random closed set. This opens the possibility to estimate geometrical and physical observables from spatial averaging within a randomly placed bounded sampling window.

For a random closed set $\mathbb{X}$ the average local volume fraction is defined as

$$\phi(\mathbf{x}) = \langle \chi_{\mathbb{X}}(\mathbf{x})\rangle \tag{7}$$

for all $\mathbf{x} \in \mathbb{R}^3$, where $\chi_{\mathbb{X}}(\mathbf{x})$ is the characteristic or indicator function of the set $\mathbb{X}$ defined as $\chi_{\mathbb{X}}(\mathbf{x}) = 1$ for $\mathbf{x} \in \mathbb{X}$ and $\chi_{\mathbb{X}}(\mathbf{x}) = 0$ for $\mathbf{x} \notin \mathbb{X}$. For stationary random closed sets it is well known that

$$\phi(\mathbf{x}) = \phi(\mathbf{x}_0) = \mu(\mathbf{x}_0 \in \mathbb{X}) = \langle V(\mathbb{X} \cap \mathbb{E})\rangle =: \phi(\mathbb{X}) \tag{8}$$

is constant and independent of $\mathbf{x}$ for every fixed $\mathbf{x}_0 \in \mathbb{R}^3$. The constant $\phi(\mathbb{X})$ is the porosity (volume fraction, volume density). More generally,

$$\phi(\mathbb{X}) = \frac{\langle V(\mathbb{X} \cap \mathbb{B})\rangle}{V(\mathbb{B})} \tag{9}$$

holds for every Borel set $\mathbb{B} \subset \mathbb{R}^3$ with $0 < V(\mathbb{B}) < \infty$. As a consequence the ratio $V(\mathbb{X} \cap \mathbb{B})/V(\mathbb{B})$ is an unbiased estimator for porosity.

The situation is less simple for other densities such as the average surface area of $\mathbb{X}$ per unit volume (specific internal surface). It may be defined as [33]

$$\sigma(\mathbb{X}) = \frac{\langle A(\mathbb{X} \cap \mathbb{B})\rangle}{V(\mathbb{B})}, \tag{10}$$

where the area

$$A(\mathbb{K}) = \int_{\partial\mathbb{K}} d\mu_2 \tag{11}$$

is well defined if $\mathbb{K}$ is the closure of its interior. Here $d\mu_2$ is the two-dimensional Hausdorff measure [34]. The first difficulty

is that the surface area $A(\mathbb{X}\cap\mathbb{B})$ is in general not defined for arbitrary Borel sets $\mathbb{B}$. For that reason the arbitrary Borel set $\mathbb{B}$ is restricted to become a convex compact "observation window" $\mathbb{W}$ with positive volume and the random closed set $\mathbb{X}$ is restricted to the extended convex ring (i.e., locally polyconvex sets). The convex and compact set $\mathbb{W}$ is also called a measurement cell. Now $\mathbb{X}\cap\mathbb{W}$ has a well-defined surface area. The second difficulty is that the surface area contains also contributions from $\mathbb{X}\cap\partial\mathbb{W}$, not only from the internal boundary of $\mathbb{X}$. Such boundary effects can be avoided by rescaling the observation window $\mathbb{W}$ to $\ell\mathbb{W}=\{\ell\mathbf{x}:\mathbf{x}\in\mathbb{W},\ell>0\}$ for large ℓ. Ideally, the density f of an observable F

$$f(\mathbb{X})=\lim_{\ell\to\infty}\frac{\langle F(\mathbb{X}\cap\ell\mathbb{W})\rangle}{V(\ell\mathbb{W})} \tag{12}$$

is obtained from an infinite-volume limit $\ell\to\infty$. For the Fontainebleau sample only a single realization exists and the expectation cannot be taken. Thus the question arises whether the pointwise limit

$$f(\mathbb{X},\omega)=\lim_{\ell\to\infty}\frac{F(\mathbb{X}(\omega)\cap\ell\mathbb{W})}{V(\ell\mathbb{W})} \tag{13}$$

exists and, if yes, whether it is a constant for almost all $\omega\in\Omega$. This is the problem of ergodicity. The convergence to the limit is related to the REV problem of how large to choose ℓ.

Answering such questions requires high-precision measurements of the geometric observables. In this paper volume and surface area are studied directly on a realistic continuum geometry with floating point accuracy.

IV. MODEL

The random closed set of the Fontainebleau model of [21] is visualized in Figs. 1 and 2. Its set of realizations Ω is the set

$$\Omega=(\mathbb{D}\times[R_{\min},R_{\max}]\times\mathbb{B}_{\mathbf{0},2\pi}\times\{1,2,\ldots,g\})^M \tag{14}$$

of all finite sequences $\omega=(\omega_1,\ldots,\omega_M)\in\Omega$ whose elements

$$\omega_i=(\mathbf{r}_i,R_i,\mathbf{a}_i,T_i),\quad i=1,\ldots,N_{\mathrm{dep}} \tag{15}$$

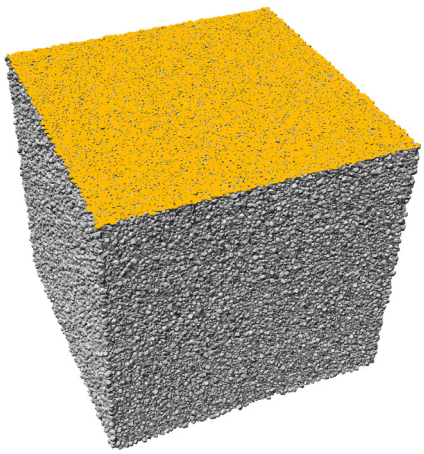

FIG. 1. (Color online) Visualization of the original grain deposit $\mathbb{U}$ in a cubic region $\mathbb{D}$ of 19.04 mm side length from which the cubic sample $\mathbb{S}$ with side length 15 mm was cropped. The cubic region shown on the image contains a total of $N_{\mathrm{dep}}=1022\,149$ grains.

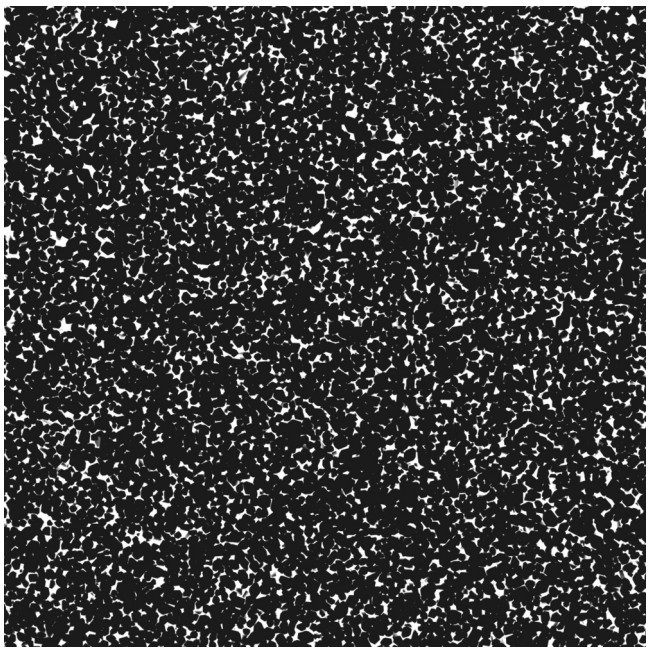

FIG. 2. Cross section with side length 15 mm of the cropped sample $\mathbb{S}\subset\mathbb{D}$. Grain matrix $\mathbb{M}$ is rendered black, pore space $\mathbb{P}$ shown in white. The sample region $\mathbb{S}$ intersects $N=534\,811$ grains of the original deposit $\mathbb{U}$.

specify position $\mathbf{r}_i\in\mathbb{D}\subset\mathbb{R}^3$, size $R_i\in[R_{\min},R_{\max}]\subset\mathbb{R}$, orientation $\mathbf{a}_i\in\mathbb{B}_{\mathbf{0},2\pi}$, and type $T_i\in\{1,2,\ldots,g\}$ of the ith grain $\mathbb{G}_i$. The deposition box (units of length are micrometers)

$$\mathbb{D}=(-170,-170,-170)^T+19\,040\mathbb{E} \tag{16}$$

is a cubic region obtained from scaling the unit cube $\mathbb{E}$ to a side length of 19 040 μm. In addition it is shifted by the vector $(-170,-170,-170)$ μm. The position $\mathbf{r}_i\in\mathbb{D}$ and size $R_i\in[R_{\min},R_{\max}]$ of a grain are identified with the center and radius of an inscribed sphere

$$\mathbb{B}_{\mathbf{r}_i,R_i}=\{\mathbf{x}\in\mathbb{R}^3:|\mathbf{x}-\mathbf{r}_i|\leqslant R_i\}. \tag{17}$$

The grain sizes R_i are chosen randomly with uniform distribution in the interval $[R_{\min},R_{\max}]$ with $R_{\min}=80$ μm, $R_{\max}=170$ μm. The grains are deposited randomly in $\mathbb{D}$ subject to certain overlap restrictions. The overlap between two grains i,j is defined as the overlap of the inscribed balls

$$O(\omega_i,\omega_j)=\frac{R_i+R_j-|\mathbf{x}_i-\mathbf{x}_j|}{R_i+R_j-|R_i-R_j|}. \tag{18}$$

The overlap obeys $0<O(\omega_i,\omega_j)\leqslant\lambda$ with $\lambda=0.158\,25$ being the maximum allowed overlap. The grains are chosen randomly with equal probability $1/g$ from $g=99$ different types of polyhedra, each having 18 faces.

The number M denotes the maximum length of the sequence. It may be chosen arbitrarily subject only to the bound given in Eq. (20) below. The random variable N_{dep} is the random number of grains deposited inside the deposition box $\mathbb{D}$. Accordingly, one defines

$$\omega_i=(\mathbf{0},0,\mathbf{0},0) \tag{19}$$

for $i = N_{\rm dep}+1,\ldots,M$ to indicate that these grains are absent. A lower bound for the maximum length M of a sequence ω can be estimated in terms of the system parameters. It depends on the volume $V(\mathbb{D})$ of the deposition box, on the minimum grain size $R_{\rm min}$, and on the maximum overlap λ. Choosing M such that

$$M > \frac{V(\mathbb{D})}{4\sqrt{2}[(1-2\lambda)R_{\rm min}]^3} \tag{20}$$

will ensure that $N_{\rm dep} < M$ holds. For the parameters $V(\mathbb{D}) = (19.04\ {\rm mm})^3$, $\lambda = 0.158\,25$, and $R_{\rm min} = 80\ \mu$m the resulting bound of $M \approx 7.5\times 10^6 > N_{\rm dep}$ is indeed much larger than the number $N_{\rm dep} \approx 10^6$ of deposited grains.

The orientation $\mathbf{a}_i \in \mathbb{B}_{\mathbf{0},2\pi}$ of a grain is specified as a rotation vector

$$\mathbf{a}_i = |\mathbf{a}_i|\mathbf{e}_i \tag{21}$$

whose orientation $\mathbf{e}_i = \mathbf{a}_i/|\mathbf{a}_i| \in \mathbb{B}_{\mathbf{0},1}$ is the rotation axis and whose length $|\mathbf{a}_i|$ is the rotation angle. The rotation matrix B corresponding to an axis-angle rotation $\mathbf{a}$ has the components b_{ij} listed in Appendix A in Eq. (A1). The orientation is chosen randomly. The parameters of its distribution are given in [21].

Note that in previous publications [6–8,21] both the mathematical and also the verbal description of the domain for $\mathbf{a}_i$ was erroneously specified as $\mathbf{a}_i \in \partial\mathbb{B}_{\mathbf{0},1}$ instead of $\mathbf{a}_i \in \mathbb{B}_{\mathbf{0},2\pi}$. We emphasize however that all computations in [6–8,21] were correctly performed based on Eq. (21) with $\mathbf{a}_i \in \mathbb{B}_{\mathbf{0},2\pi}$ so that the reported results remain unchanged and correct.

The Borel σ algebra $\mathcal{O}$ of the underlying probability space $(\Omega,\mathcal{O},\mu)$ is the product algebra of the Borel σ algebras of its factors (for the types $\{1,2,\ldots,g\}$ this is the power set). Figure 1 shows the realization $\mathbb{U}(\omega)$ of the random closed set from [21] that is studied here. It consist of $N_{\rm dep} = 1\,022\,149$ randomly positioned partially overlapping grains of random size, orientation, and type. Their union

$$\mathbb{U} = \bigcup_{i=1}^{N_{\rm dep}} \mathbb{G}_i \tag{22}$$

is a polyconvex random closed set.[1] To eliminate boundary effects a cubic sample region $\mathbb{S} \subset \mathbb{D}$ of side length 1.5 cm was cropped from the realization $\mathbb{U}(\omega)$. The intersection

$$\mathbb{M}(\omega) = \mathbb{S} \cap \mathbb{U}(\omega) \tag{23}$$

is the grain matrix. The pore space inside $\mathbb{S}$ is defined as

$$\mathbb{P}(\omega) = \overline{\mathbb{S} \setminus \mathbb{M}(\omega)}; \tag{24}$$

the closure of the complement of $\mathbb{M}(\omega)$ in $\mathbb{S}$. $\mathbb{P}(\omega)$ denotes again the realization of the random closed set $\mathbb{P} = \overline{\mathbb{S}\setminus\mathbb{M}}$. The grain matrix $\mathbb{M}(\omega)$ of the cropped sample contains $N = 534\,811$ grains. A cross section is shown in Fig. 2. In the figure the grains are shown in black, the pores in white.

The parameters of the random closed set $\mathbb{U}$ were calibrated geometrically in [21] to match the geometric properties of Fontainebleau sandstone. An experimental microtomogram at 7.5 μm resolution was available from [25]. The geometric calibration was based on matching volume fraction (porosity), specific surface, integrated mean curvature, Gaussian curvature, two-point-correlation function, local porosity distributions (with 240 μm and 480 μm measurement cell size), and local percolation probabilities at the same measurement cell sizes. The comparison of these quantities at $a = 7.5\ \mu$m is given in [21].

In [21,22] the sample $\mathbb{S}$ was discretized into N cubic voxels $\mathbb{V}_i(a) \subset \mathbb{S}$ $(i = 1,\ldots,N)$, whose side length a is a multiple of the base resolution $a_0 = 1.5\ {\rm cm}/16\,384 = 0.915\,527\,3\ \mu$m. Nine different resolutions $a = a_0/2, a_0, 2a_0, 4a_0, 8a_0, 16a_0, 32a_0, 64a_0, 128a_0$ were used to compute resolution-dependent properties in [22]. The porosity was obtained as $13.431 \pm 0.001\%$. The specific internal surface area was estimated as $10.35 \pm 1.34\ {\rm mm}^{-1}$. The permeability of a subsample of size $(300)^3$ was found as 1182 mD in [21].

V. METHOD

The method of binary space partitioning (BSP trees) [35, Chap.,12] was suggested and used in [36] to compute the volume of the pore space. This method suffers from large memory requirements, low speed, and lack of precision. Binary space partitioning failed to compute the precise volume for the Fontainebleau sample [36].

The method adopted in this paper is based on the general formula [37]

$$\begin{aligned} V(\mathbb{M}\cap\mathbb{W}) &= V\left(\bigcup_{i=1}^{N}\widetilde{\mathbb{G}}_i\right) \\ &= \sum_{\mathbb{I}\in\mathcal{P}(N)} (-1)^{|\mathbb{I}|-1}\, V\left(\bigcap_{i\in\mathbb{I}}\widetilde{\mathbb{G}}_i\right), \end{aligned} \tag{25}$$

valid not only for volume, but for any additive set functional [33]. In Eq. (25) the sets

$$\widetilde{\mathbb{G}}_i = \mathbb{G}_i \cap \mathbb{W} \tag{26}$$

denote the grains $\mathbb{G}_i$ restricted to a bounded, rectangular polyhedral window $\mathbb{W} \subset \mathbb{S}$. The integer N is the number of grains $\mathbb{G}_i \subset \mathbb{R}^3$, $V(\mathbb{G})$ denotes the volume (Lebesgue measure) of a subset $\mathbb{G} \subset \mathbb{R}^3$, $|\mathbb{I}|$ the cardinality of the index set $\mathbb{I} \in \mathcal{P}(N)$, and $\mathcal{P}(N)$ the set of all nonempty subsets of the set $\{1,\ldots,N\}$ [37]. Equation (25) combined with the fact that the intersection of two convex compact polyhedra is again a convex compact polyhedron [38] allows the computation of $V(\mathbb{M}\cap\mathbb{W})$ to be reduced to the computation of the volume of convex and compact polyhedra as will be shown next.

Given any $j = 1,\ldots,N$ the recursive algorithm transforms the set $\{\mathbb{G}_1,\ldots,\mathbb{G}_j\}$ of original grains into a set

$$\mathcal{L}_j = \left\{(\mathbb{K}_1,\zeta_1),\ldots,\left(\mathbb{K}_{Z_j},\zeta_{Z_j}\right)\right\} \tag{27}$$

of pairs. Each pair $(\mathbb{K},\zeta)$ consists of a grain (polyhedron) $\mathbb{K}$ and an indicator $\zeta = \pm 1$. For $j = 0$ define $\mathcal{L}_0 = \emptyset$ to be the empty set. Given $\mathcal{L}_{j-1}$, the set $\mathcal{L}_j$ is constructed iteratively as follows:

(1) If $j \leqslant N$, compute the volume $V(\widetilde{\mathbb{G}}_j)$, else stop.

[1] Convex and compact sets are called convex bodies [33]. Finite unions of convex bodies are called polyconvex sets. The set of polyconvex sets is called the convex ring $\mathcal{R}$.

(2) If $V(\widetilde{\mathbb{G}}_j) = 0$, increment j by 1 and return to (1).
(3) If $V(\widetilde{\mathbb{G}}_j) \neq 0$, then
  (a) set $\mathbb{K}_{Z_{j-1}+1} = \widetilde{\mathbb{G}}_j$, $\zeta_{Z_{j-1}+1} = 1$ and add the pair $(\mathbb{K}_{Z_{j-1}+1}, \zeta_{Z_{j-1}+1})$;
  (b) set $i = k = 1$;
  (c) if $i \leqslant Z_{j-1}$ compute $V(\mathbb{K}_i \cap \widetilde{\mathbb{G}}_j)$ else increment j by 1 and return to (1);
  (d) if $V(\mathbb{K}_i \cap \widetilde{\mathbb{G}}_j) = 0$ increment i by 1 and return to (3c);
  (e) if $V(\mathbb{K}_i \cap \widetilde{\mathbb{G}}_j) \neq 0$ set $\zeta_{Z_{j-1}+1+k} = -\zeta_i$ and $\mathbb{K}_{Z_{j-1}+1+k} = \mathbb{K}_i \cap \widetilde{\mathbb{G}}_j$ and add the pair $(\mathbb{K}_{Z_{j-1}+1+k}, \zeta_{Z_{j-1}+1+k})$;
  (f) increment i by 1, increment k by 1, go to (3c).

To reduce the computational cost of determining the intersections in step (3), the region $\mathbb{W}$ is decomposed into cubic cells whose side length is the diameter of the smallest sphere containing the largest grain. In this way only grains within the same cell as the cell containing grain $\widetilde{\mathbb{G}}_j$ and within its 26 neighboring cells need to be checked for nonzero intersection. This decreases the numerical effort enormously, especially for large systems with many thousands of grains.

The total volume of the pore space $\mathbb{P}$ inside the measurement cell $\mathbb{W}$ can now be computed from the set $\mathcal{L}_N$ of pairs as

$$V(\mathbb{P} \cap \mathbb{W}) = V(\mathbb{W}) - \sum_{j=1}^{Z_N} \zeta_j V(\mathbb{K}_j) \tag{28}$$

by computing all $V(\mathbb{K}_j)$ with $j = 1, \ldots, Z_N$. Because every $\mathbb{K}_j$ is the intersection of two convex and compact polyhedra it is itself a convex and compact polyhedron [38]. The algorithm for computing the volume $V(\mathbb{K}_j)$ for arbitrary convex and compact polyhedra is detailed in Appendix B.

VI. RESULTS

A. Precision measurements

Figure 3 shows porosity data for the continuum Fontainebleau model. With an accuracy of 15 significant digits the numerical uncertainty of the data is much smaller than the linewidth. The four curves trace the porosity inside four cubic measurement windows

$$\mathbb{W}_1(\ell) = (L-\ell,0,0)^T + \ell\mathbb{E}, \tag{29a}$$
$$\mathbb{W}_2(\ell) = (L-\ell,0,L-\ell)^T + \ell\mathbb{E}, \tag{29b}$$
$$\mathbb{W}_3(\ell) = (L-\ell,L-\ell,0)^T + \ell\mathbb{E}, \tag{29c}$$
$$\mathbb{W}_4(\ell) = (L-\ell,L-\ell,L-\ell)^T + \ell\mathbb{E}, \tag{29d}$$

whose side lengths ℓ increase from 2 to 15 000 μm in steps of 2 μm. Each of the four curves

$$\phi_i(\ell) = \frac{V(\mathbb{P} \cap \mathbb{W}_i(\ell))}{V(\mathbb{W}_i(\ell))} \tag{30}$$

with $i = 1$ (black), $i = 2$ (green), $i = 3$ (red), and $i = 4$ (blue) corresponds to a different corner of $\mathbb{S}$ from which the cubic windows are grown towards the opposite corner along the space diagonals of $\mathbb{S}$. All four curves converge to the full sample $\mathbb{W}_i(L) = L\mathbb{E} = \mathbb{S}$. Its porosity was computed with

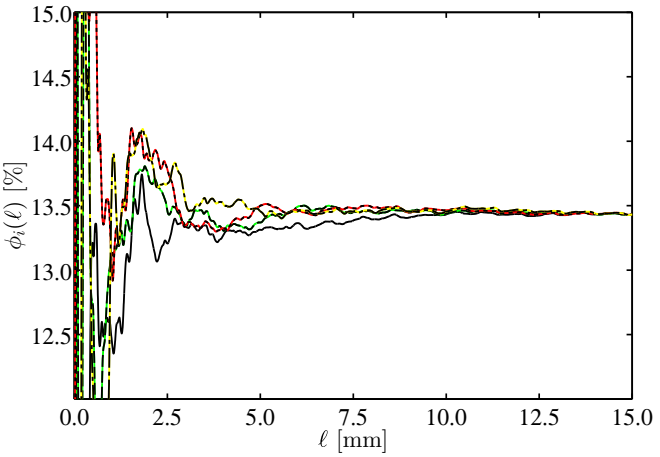

FIG. 3. (Color online) Porosity $\phi_i(\ell), i = 1,2,3,4$ of the 15 mm sample $\mathbb{S}$ shown in Fig. 2 as a function of measurement cell size ℓ for four cubic measurement cells $\mathbb{W}$ increasing from four corners to the full sample $\mathbb{S}$ along a space diagonal. Specifically, the measurement cells are $\mathbb{W}_1(\ell) = (L-\ell,0,0)^T + \ell\mathbb{E}$ (black, solid), $\mathbb{W}_2(\ell) = (L-\ell,0,L-\ell)^T + \ell\mathbb{E}$ [black (green), dashed], $\mathbb{W}_3(\ell) = (L-\ell,L-\ell,0)^T + \ell\,\mathbb{E}$ [black (red), dotted], and $\mathbb{W}_4(\ell) = (L-\ell,L-\ell,L-\ell)^T + \ell\,\mathbb{E}$ [black (yellow), dash-dotted].

floating point precision as

$$\phi_i(L) = \phi(\mathbb{S}) = 13.431\,010\,133\,598\,4\% \tag{31}$$

with an uncertainty of at most ± 1 in the last digit.

Figure 4 shows the pore surface area per unit volume

$$\sigma_i(\ell) = \frac{A(\mathbb{P} \cap \mathbb{W}_i(\ell))}{V(\mathbb{W}_i(\ell))} \tag{32}$$

for the same four suites of measurement cells $\mathbb{W}_i(\ell)$ as in Fig. 3. The pore surface area density of the full sample to which all four curves converge for $\ell = L$ is

$$\sigma_i(L) = \sigma(\mathbb{S}) = 10.473\,444\,544\,162\,2\ \text{mm}^{-1} \tag{33}$$

with an uncertainty of at most ± 1 in the last digit.

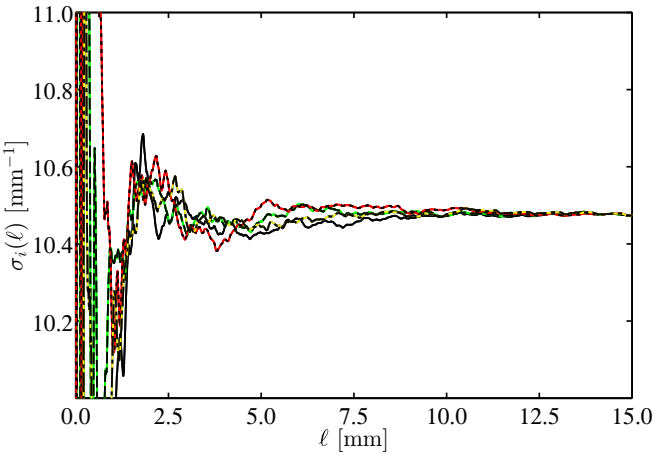

FIG. 4. (Color online) Internal surface area density $\sigma_i(\ell)$ of the Fontainebleau sample $\mathbb{S}$ as a function of measurement window size ℓ for the same four cubic measurement cells as in Fig. 3. Colors are identical to those in Fig. 3.

B. REV plots

Plots similar to Fig. 3 are often used in a schematic way without actual data to illustrate the idea of a representative elementary volume for porosity or other observables [39, p.60, Fig. 4.3]. Figures 3 and 4 suggest that the REV length is around 10 mm for both porosity and surface area density.

Both plots seem to show that the sample is very homogeneous. Experimental specimens of Fontainebleau sandstone are typically much more heterogeneous than our continuum model. It turns out, however, that the homogeneity seen in Figs. 1, 2, 3, and 4 is deceptive. The sample is less homogeneous than it appears to the eye. Strong fluctuations and unexpected correlations can be detected by differential porosimetry. This illustrates the importance of high-precision analysis for REV studies.

C. Differential porosimetry

Instead of plotting the porosities $\phi_i(\ell)$ against ℓ it is instructive to consider the volume $V(\mathbb{P}\cap\mathbb{W}_i(\ell))$ as a function of the averaging volume $V(\mathbb{W}_i(\ell))$. This approach suggestscomparison of the average porosity inside the averaging window defined in Eq. (30) to the differential porosity defined as

$$\psi_i = \frac{d\,V(\mathbb{P}\cap\mathbb{W}_i(\ell))}{dV(\mathbb{W}_i(\ell))}, \tag{34}$$

i.e., $\psi_i = du_i/dv_i$, where $u_i = V(\mathbb{P}\cap\mathbb{W}_i(\ell))$ is considered as a function $u_i(v_i)$ of $v_i = V(\mathbb{W}_i(\ell))$. The comparison is shown in Fig. 5.

The same comparison is shown in Fig. 6 for internal surface area and differential internal surface area

$$\tau_i = \frac{dA(\mathbb{P}\cap\mathbb{W}_i(\ell))}{dV(\mathbb{W}_i(\ell))}, \tag{35}$$

where $A(\mathbb{P}\cap\mathbb{W}_i(\ell)) = u_i$ is considered as a function $u_i(v_i)$ of $v_i = V(\mathbb{W}_i(\ell))$. Both figures show strong fluctuations in the differential porosity (respectively differential internal surface area) when their spatial averages are essentially constant.

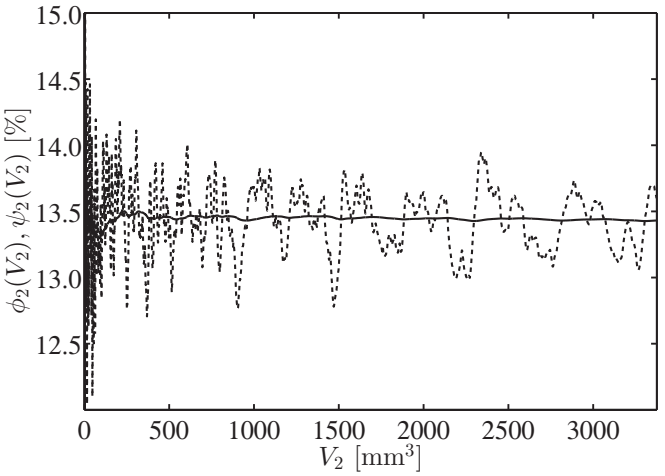

FIG. 5. Comparison of porosity $\phi_2(V_2)$ (solid curve) and differential porosity $\psi_2(V_2)$ (dashed curve) as functions of the volume $V_2 = V(\mathbb{W}_2(\ell))$ defined in Eq. (29b).

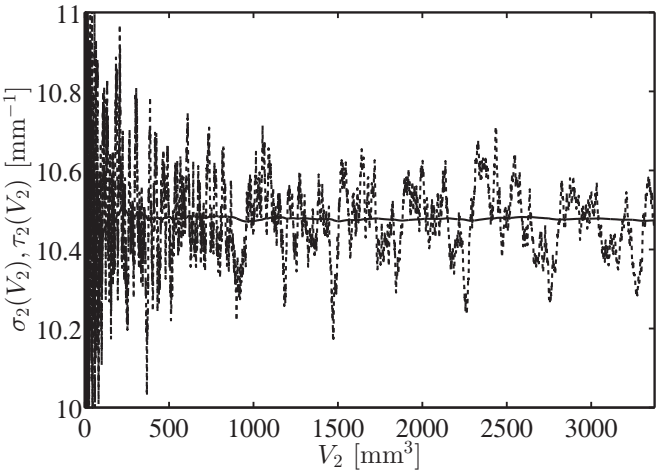

FIG. 6. Comparison of specific internal surface area $\sigma_2(V_2)$ (solid curve) and differential internal surface area $\tau_2(V_2)$ (dashed curve) as functions of the averaging volume $V_2 = V(\mathbb{W}_2(\ell))$ of the averaging window defined in Eq. (29b).

These fluctuations become even more pronounced when the averaging windows are chosen such that the averaging volumes become equidistant. Let

$$\mathbb{W}_x(\ell) = \mathbb{W}(\ell, L, L), \tag{36a}$$

$$\mathbb{W}_y(\ell) = \mathbb{W}(L, \ell, L), \tag{36b}$$

$$\mathbb{W}_z(\ell) = \mathbb{W}(L, L, \ell), \tag{36c}$$

where

$$\mathbb{W}(\ell_x, \ell_y, \ell_z) = [0, \ell_x] \times [0, \ell_y] \times [0, \ell_z] \tag{37}$$

denotes a rectangular parallelepiped (cuboid) with side lengths ℓ_x, ℓ_y, ℓ_z. Let $\phi_x(V_x)$ denote the porosity defined from Eq. (30) with $i = x$ as a function of $V_x = V(\mathbb{W}_x(\ell))$. The corresponding differential porosity is denoted as $\psi_x(V_x)$ and similarly for internal surface area $\sigma_x(V_x)$ and its differential $\tau_x(V_x)$. Figures 7 and 8 show the results. Similar plots are obtained along

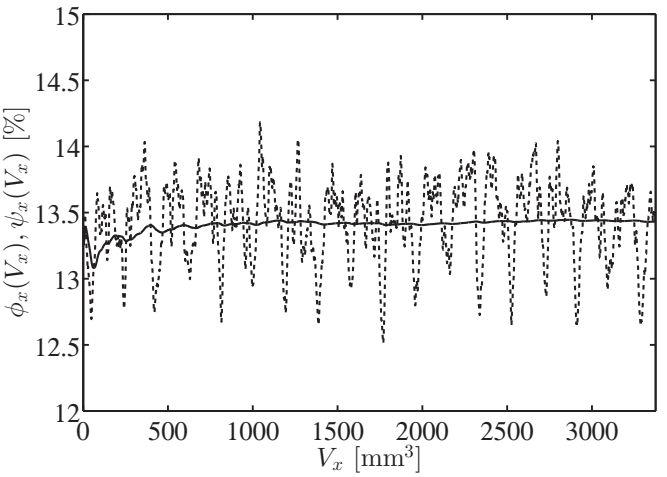

FIG. 7. Porosity $\phi_x(V_x)$ and differential porosity $\psi_x(V_x)$ for equidistant averaging volumes V_x.

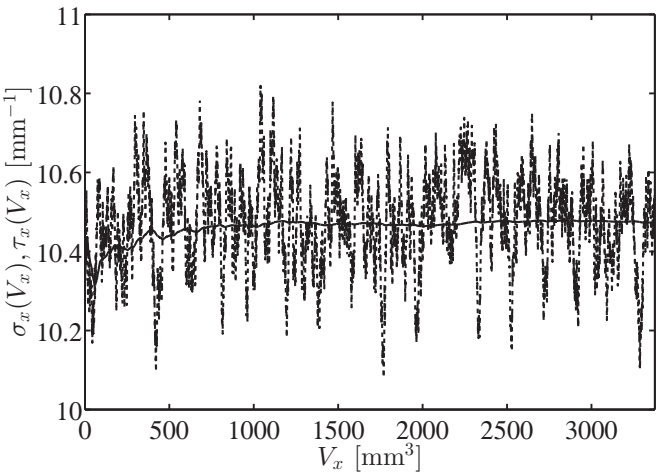

FIG. 8. Internal surface area $\sigma_x(V_x)$ and differential internal surface area $\tau_x(V_x)$ for equidistant averaging volumes V_x.

the y or z direction. Apart from strong random fluctuations a periodic oscillation is clearly observed in these plots. Fourier analysis confirms the periodicity and gives a period of 850 μm corresponding to five times the maximum grain size.

Figure 9 plots the differential surface area density against the differential porosity for the curves $\psi_x(V_x)$ and $\tau_x(V_x)$ shown in Figs. 7 and 8 in the range $1688\ \text{mm}^{-1} \leqslant V_x \leqslant 3375\ \text{mm}^{-1}$. The numerical uncertainty is much smaller than the symbol size in Fig. 9. The last point for $V_x = 3375\ \text{mm}^{-1}$ corresponds to the full sample and it is marked by a green (light gray) square. The red (gray) line is a power-law fit to the data of the form $\tau = a\psi^b$. The fit parameters are $a = 3.767\ \text{mm}^{-1}$ and $b = 0.394$. Figure 9 illustrates and emphasizes the fact that there does not exist a unique relation between σ and ϕ despite their strong correlation.

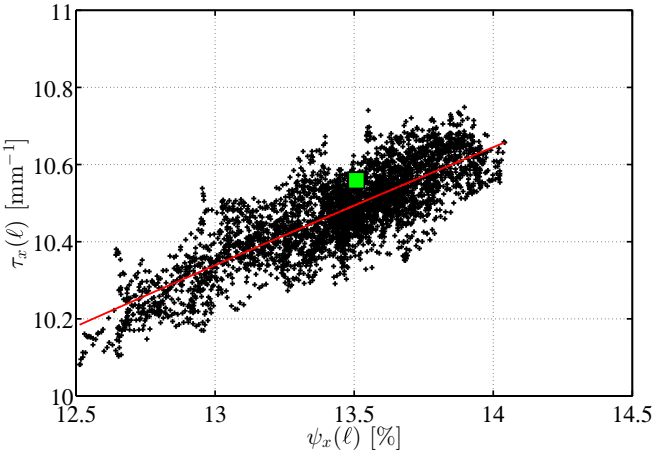

FIG. 9. (Color online) Differential internal surface area density versus differential porosity for the last half of the curves $\psi_x(V_x)$ and $\tau_x(V_x)$ shown in Figs. 7 and 8. The last point corresponding to the full sample is shown as the center of the green (light gray) square. The red (gray) line shows a fit of the function $\tau = a\psi^b$ with $a = 3.767\ \text{mm}^{-1}$ and $b = 0.394$ to the data.

D. Comparison to synthetic μ-CT

The observation of periodic oscillations by differential porosimetry raises the question whether these oscillations can also be observed in traditional nondifferential porosimetry, perhaps even in discrete approximations, for sufficiently high precision. To answer this question the discretized and thresholded approximation available as the set of files a8*.gbd.gz from [40] will be used.

The discretized approximation to the continuum geometry has a total porosity of

$$\widetilde{\phi}(\mathbb{S}) = 13.4319\% \tag{38}$$

and a surface area density of

$$\widetilde{\sigma}(\mathbb{S}) = 9.2938\ \text{mm}^{-1} \tag{39}$$

as measured with the algorithms described in [41]. While the porosity agrees with Eq. (31) to five digits the area density differs from Eq. (33) already in the first digit. Accordingly, the relative errors are only

$$\frac{\Delta\phi(\mathbb{S})}{\phi(\mathbb{S})} = \frac{|\widetilde{\phi}(\mathbb{S}) - \phi(\mathbb{S})|}{\phi(\mathbb{S})} \approx 0.0066\% \tag{40}$$

for porosity and

$$\frac{\Delta\sigma(\mathbb{S})}{\sigma(\mathbb{S})} = \frac{|\widetilde{\sigma}(\mathbb{S}) - \sigma(\mathbb{S})|}{\sigma(\mathbb{S})} \approx 11.263\% \tag{41}$$

for internal surface area density. The large absolute difference

$$\Delta\sigma(\mathbb{S}) = 1.179\,61\ \text{mm}^{-1} \tag{42}$$

results from the discretization of flat polyhedral faces on a structured cubic grid.

Figure 10 shows the comparison between the continuum model and its discretized and thresholded approximation at a resolution of 7.3242 μm. The discretized sample is available as file set a8*.gbd.gz from [40] for download. Figure 10 shows four curves: the continuum porosity $\phi_x(\ell) = \phi(\mathbb{W}_x(\ell)) = \phi(\mathbb{W}(\ell, L, L))$ and the discrete porosity $\phi_x(\ell) = \phi(\mathbb{W}_x(\ell)) = \phi(\mathbb{W}(\ell, L, L))$ for exactly the same suite of measurement windows with $10 \leqslant \ell \leqslant 15$ mm. The porosities are shown as black curves on the bottom and they have their ordinate (vertical axis) on the left. Note the reduced range of values on the abscissa. The continuum surface area density $\sigma_x(\ell) = \sigma(\mathbb{W}_x(\ell)) = \sigma(\mathbb{W}(\ell, L, L))$ for $10 \leqslant \ell \leqslant 15$ mm is shown as a blue solid line on top with ordinate on the right. The blue line with open square symbols on the top is the discrete surface area density $\widetilde{\sigma}_x(\ell) = \widetilde{\sigma}(\mathbb{W}_x(\ell)) = \widetilde{\sigma}(\mathbb{W}(\ell, L, L))$ for $10 \leqslant \ell \leqslant 15$ mm rescaled by a factor $\sigma(\mathbb{S})/\widetilde{\sigma}(\mathbb{S}) \approx 1.112\,63$ to correct for the discretization error.

It is seen that the discrete porosity overestimates the true continuum porosity. On the other hand the fluctuations due to the random geometry are reproduced faithfully. Remarkably, the same holds for the surface area density. Despite the large discretization error of 11% the geometric changes produce identical fluctuations of the discrete and continuum measurement. This shows that the discretization provided in a8*.gbd.gz is a faithful representation of the continuum model. The continuum model as well as its discretization clearly show small oscillations in porosity and surface area density with a period of roughly 850 μm.

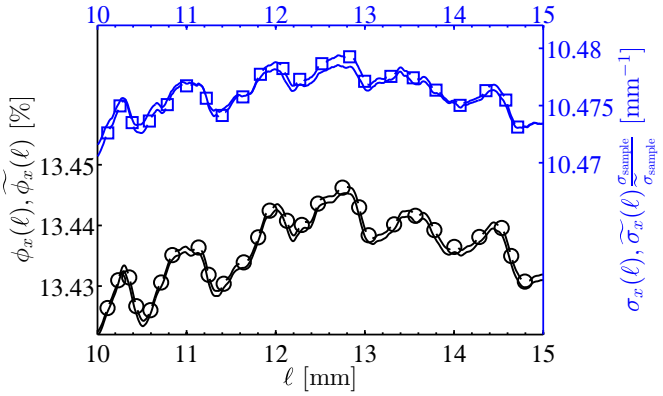

FIG. 10. (Color online) Continuum porosity $\phi_x(\ell)$ (lower black solid line) and discrete porosity $\widetilde{\phi}_x(\ell)$ (lower black line with open circles) are shown on the bottom with $10 \leqslant \ell \leqslant 15$ mm on the abscissa and their ordinate on the left. Continuum internal surface area density $\sigma_x(\ell)$ [upper blue (gray) solid line] and rescaled discrete surface area density $\widetilde{\sigma}_x(\ell)\sigma(\mathbb{S})/\widetilde{\sigma}(\mathbb{S})$ [upper blue (gray) line with open squares] are shown on the top with $10 \leqslant \ell \leqslant 15$ mm on the abscissa and their ordinate on the right. The lines with symbols (open circles and open squares) refer to the discretization a8*.gbd.gz from [40] with a resolution of $8 \times 15\,000/16\,384 = 7.3242$ μm. The solid lines show floating point precision results evaluated in steps of $\Delta\ell = 8 \times 15\,000/16\,384 = 7.3242$ μm corresponding to the side length of one voxel in the discretized image.

E. Thin section analysis

Experimentally one often has only a few thin sections available for analysis. Quasi-two-dimensional thin sections are routinely prepared experimentally and are easily evaluated computationally with our algorithm. If the continuum model is indeed homogeneous (stationary) then standard theorems of stereology [33,42] predict that porosity and internal surface area density can also be measured from thin sections. If the medium is also ergodic then the validity of Eq. (13) for almost all $\omega \in \Omega$ implies that large thin sections are sufficient.

To test ergodicity and the validity of Eq. (13) for ϕ or σ the following five different thin sections of height $\Delta z = 2a_0 \approx 1.8$ μm have been selected along the z axis:

$$\mathbb{W}_0(\ell) = \mathbb{W}(\ell,\ell,2a_0), \tag{43a}$$
$$\mathbb{W}_{1831.1}(\ell) = (0,0,1831.1)^T + \mathbb{W}(\ell,\ell,2a_0), \tag{43b}$$
$$\mathbb{W}_{4577.6}(\ell) = (0,0,4577.6)^T + \mathbb{W}(\ell,\ell,2a_0), \tag{43c}$$
$$\mathbb{W}_{6207.3}(\ell) = (0,0,6207.3)^T + \mathbb{W}(\ell,\ell,2a_0), \tag{43d}$$
$$\mathbb{W}_{9036.3}(\ell) = (0,0,9036.3)^T + \mathbb{W}(\ell,\ell,2a_0). \tag{43e}$$

These five different thin sections $\mathbb{P}(\omega) \cap \mathbb{W}_i(\ell)$ with $i \in \{0,1831.1,4577.6,6207.3,9036.3\}$ may be viewed as five different realizations ω_i in $\mathbb{W}_0(\ell) = \mathbb{W}(\ell,\ell,2a_0)$. The question becomes whether the size L of the sample is large enough for

$$\phi(\mathbb{P},\omega_i) = \lim_{\ell\to\infty} \frac{V(\mathbb{P}(\omega) \cap \mathbb{W}_i(\ell))}{V(\mathbb{W}_i(\ell))} \approx \frac{V(\mathbb{P}(\omega) \cap \mathbb{W}_i(L))}{V(\mathbb{W}_i(L))} \tag{44}$$

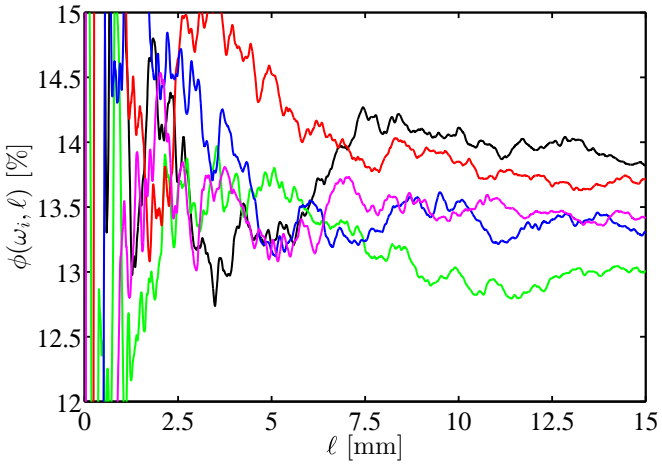

FIG. 11. (Color online) Porosity traces $\phi(\omega_i,\ell)$ of the 15 mm sample $\mathbb{S}$ shown in Fig. 2 as functions of measurement cell size ℓ for five different thin sections ω_i. The thin sections had a height of $\Delta z = 2a_0 \approx 1.8$ μm and are colored as $i = 0$ (black), $i = 1831.1$ [green (very light gray)], $i = 4577.6$ [red (gray)], $i = 6207.3$ [blue (dark gray)], and $i = 9036.3$ [magenta (light gray)]. At $\ell = 15$ the line order from top to botton is black, red, magenta, blue, green.

to equal $\langle V(\mathbb{P} \cap \mathbb{W}_0(\infty))\rangle / V(\mathbb{W}_0(\infty))$ independent of i. Figure 11 shows the five curves

$$\phi(\omega_i,\ell) = \frac{V(\mathbb{P}(\omega) \cap \mathbb{W}_i(\ell))}{V(\mathbb{W}_i(\ell))} \tag{45}$$

with $i = 0$ (black), $i = 1831.1$ (green), $i = 4577.6$ (red), $i = 6207.3$ (blue), and $i = 9036.3$ (magenta) as a function of ℓ for $0 \leqslant \ell \leqslant L$. It is clearly seen that the fluctuations are of the same order as those of the differential porosity in Fig. 7. This shows that the results still depend on i at this system size. Combined with the results for the differential porosity this suggests estimating the total porosity as

$$\phi(\mathbb{S}) \approx 13.4 \pm 1.0\%, \tag{46}$$

where the uncertainty is mainly attributed to geometric fluctuations.

For experimentally obtained thin sections it is not easy to obtain the surface area density, but this can be done easily here. The results for

$$\sigma(\omega_i,\ell) = \frac{A(\mathbb{P}(\omega) \cap \mathbb{W}_i(\ell))}{V(\mathbb{W}_i(\ell))} \tag{47}$$

are shown in Fig. 12. Combined with the differential results from Fig. 8 the surface area density of the 15 mm sample is estimated as

$$\sigma(\mathbb{S}) \approx 10.5 \pm 0.3 \text{ mm}^{-1}, \tag{48}$$

where the uncertainty is attributed to geometric fluctuations due to insufficient spatial self-averaging.

F. Differential permeametry

Encouraged by the good agreement between continuum and lattice discretization seen in Fig. 10, it seems promising to introduce differential permeabilities analogous to the differential porosities. Even though permeability can at present

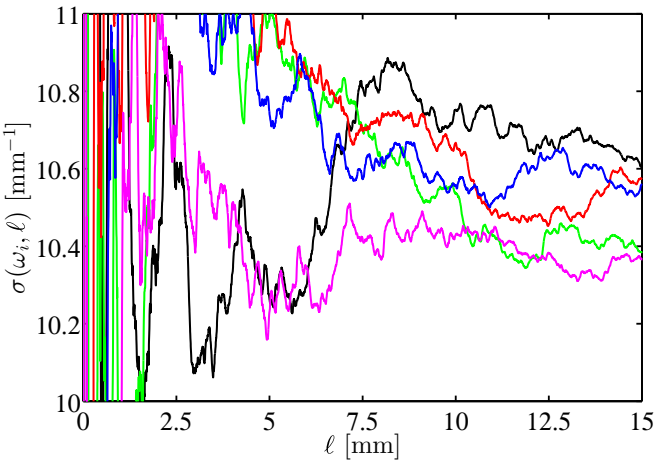

FIG. 12. (Color online) Traces of surface area density $\sigma(\omega_i,\ell)$ of the 15 mm sample $\mathbb{S}$ shown in Fig. 2 as functions of measurement cell size ℓ for five different thin sections ω_i. The thin sections had a height of $\Delta z = 2a_0 \approx 1.8$ μm and are colored as $i = 0$ (black), $i = 1831.1$ [green (very light gray)], $i = 4577.6$ [red (gray)], $i = 6207.3$ [blue (dark gray)], and $i = 9036.3$ [magenta (light gray)]. At $\ell = 15$ the line order from top to botton is black, red, blue, green, magenta.

not be computed precisely for the continuum model, it can be computed for discretized approximations, and the impressive agreement in Fig. 10 suggests that at least the variations of permeability as functions of ℓ will be accurate.

The permeability is obtained by solving Eq. (1) in a region $\mathbb{W}$ and integrating the velocity field

$$\mathbf{w}(\mathbb{W}) = \int_{\mathbb{W}} \mathbf{v}(\mathbf{x})\, d^3\mathbf{x} \tag{49}$$

for several different boundary conditions. As in experiment, the permeability is estimated from computing the volume flux per unit area as

$$k_{\partial\mathbb{S}_\mathrm{i},\partial\mathbb{S}_\mathrm{o}}(\mathbb{S}) = \frac{|\mathbf{w}(\mathbb{S})|}{V(\mathbb{S})} = \frac{1}{V(\mathbb{S})}\left|\int_{\mathbb{S}} \mathbf{v}(\mathbf{x})\, d^3\mathbf{x}\right| \tag{50}$$

where $\mathbf{v} = (v_x, v_y, v_z)^T$ is the solution of Eq. (1) with inlet $\partial\mathbb{S}_\mathrm{i}$ and outlet $\partial\mathbb{S}_\mathrm{o}$. The lower index on k is added to indicate explicitly the implicit dependence of $\mathbf{v}$ on the inlet $\partial\mathbb{S}_\mathrm{i}$ and outlet $\partial\mathbb{S}_\mathrm{o}$.

Differential permeabilities are introduced analogous to the differential porosities as

$$\kappa = \frac{d\,|\mathbf{w}(\mathbb{W}(\ell))|}{d\,V(\mathbb{W}(\ell))} \tag{51}$$

for a suitable family $\mathbb{W}(\ell)$ of windows. Again they depend implicitly via $\mathbf{v}$ on the inlet $\partial\mathbb{S}_\mathrm{i}$ and the outlet $\partial\mathbb{S}_\mathrm{o}$. Differential permeabilities can be measured experimentally by grinding thin slices from a cubic sample.

Equation (1) was formulated as a faithful model of experimental permeability measurements. In experiments the sample is typically enclosed with impermeable walls perpendicular to the applied pressure gradient. The permeability is thus a scalar quantity that depends on the choice of boundary conditions. Estimating the full permeability tensor requires different boundary conditions or volume respectively disorder averaging of pore scale velocities and pressure gradients over subregions. For a detailed discussion and comparison see [43]. Here we use the results from precision porosimetry to estimate the magnitude and fluctuations of the permeability using experimentally observed correlations.

Various functional relations of the form $k = k(\phi)$ or $k = k(\phi,\sigma)$ have been proposed according to Eq. (2) for Fontainebleau sandstone [28,44,45]. The relation

$$k_{\mathrm{BZ}}(\phi) = \left(\frac{\delta}{\delta_0}\right)^2 0.303(100\ \phi)^{3.05}\ \mathrm{mD}, \tag{52}$$

where 1 mD denotes 1 millidarcy$= 10^{-15}$ m^2, is adapted from [46] for the range $0.09 \leqslant \phi \leqslant 0.28$. The improved relation for the range $0.04 \leqslant \phi \leqslant 0.25$,

$$k_{\mathrm{ZP}}(\phi) = \left(\frac{\delta}{\delta_0}\right)^2 \frac{10^{11.17(\log 100\phi)^3+51.6\lg 100\phi}}{10^{40.29(\log 100\phi)^2+20.22}}\ \mathrm{mD}, \tag{53}$$

where log is the logarithm with base 10, stems from [28]. Both relations apply for a mean grain diameter $\delta_0 = 250$ μm and the prefactor corrects for a deviation from the mean grain diameter. The Kozeny-Carman relation [29] for a bundle of nonintersecting capillary tubes reads

$$k_{\mathrm{KC}}(\phi,\sigma) = \frac{\phi^3}{G\mathcal{T}^2\sigma^2}\ \mathrm{D} \tag{54}$$

where D denotes 1 darcy$= 10^{-12}$ m^2, σ is given in m^{-1}, $\mathcal{T}$ denotes the tortuosity, and G is the shape factor for the tube cross section. For capillary tube models the tortuosity is the ratio of tube lengths to L. For granular media, such as sands or high-porosity Fontainebleau sandstone, the Kozeny-Carman relation is often applied by eliminating $\mathcal{T}\sigma$ with

$$\mathcal{T}\sigma = \frac{1}{N}\sum_{i=1}^{N}\frac{A(\mathbb{G}_i)}{V(\mathbb{G}_i)}, \tag{55}$$

the average specific surface area of the grains [29]. Accounting for the existence of a percolation threshold at $\phi = \phi_p$ as suggested in [45], one arrives at the form

$$k_{\mathrm{MN}}(\phi) = \frac{1}{GN^2}\left(\sum_{i=1}^{N}\frac{V(\mathbb{G}_i)}{A(\mathbb{G}_i)}\right)^2 \frac{(\phi-\phi_p)^3}{(1-\phi+\phi_p)^2}\ \mathrm{D} \tag{56}$$

where V and A are measured in m^3 and m^2, respectively.

To compare these functional forms quantitatively against numerical solutions of Eq. (1) several choices for the average grain diameter δ come to mind. The mean of the uniform distribution of grain sizes is $(R_{\max}+R_{\min})/2 = 125$ μm, giving 250 μm as the diameter of an inscribed sphere for all types of grains. The equivalent diameter based on grain volume is

$$\delta_v = \frac{250\ \mu\mathrm{m}}{99}\sum_{i=1}^{99}\left(\frac{3V\left(\mathbb{G}_i^0\right)}{4\pi}\right)^{1/3} \approx 295\ \mu\mathrm{m}, \tag{57}$$

where $\mathbb{G}_i^0$ $i = 1,\ldots,99$ denotes the grain templates (see Appendix B). The equivalent diameter based on the surface

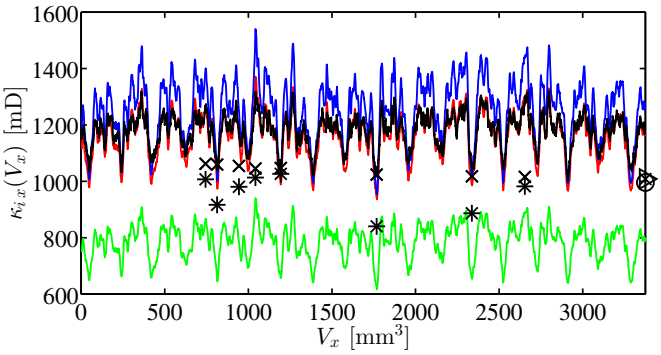

FIG. 13. (Color online) Differential permeabilities $\kappa_{i\,x}$ (solid lines) of the continuum model estimated from Eqs. (52)–(56) with $i = \mathrm{BZ}$ [red (gray)], $i = \mathrm{ZP}$ [green (very light gray, fluctuating around 800 mD], $i = \mathrm{KC}$ (black), $i = \mathrm{MN}$ [blue (dark gray)] as functions of increasing averaging volume. The lines for $i = \mathrm{BZ}$ and $i = \mathrm{KC}$ follow each other closely, $i = \mathrm{MN}$ lies systematically above, and $i = \mathrm{ZP}$ systematically below. The symbols are the permeabilities $\widetilde{k}_{xx}$ (crosses) and differential permeabilities $\widetilde{\kappa}_{xx}$ (stars) for the discretization a8*.gbd.gz obtained from numerical solution of Eq. (1) using the massively parallel algorithm of [47]. On the right axis the permeabilities $\widetilde{k}_{xx}$ (cross), $\widetilde{k}_{yy}$ (triangle), and $\widetilde{k}_{zz}$ (circle) for the full discretized sample are shown.

area of grains is

$$\delta_a = \frac{250\ \mu\mathrm{m}}{99} \sum_{i=1}^{99} \left(\frac{A\left(\mathbb{G}_i^0\right)}{4\pi} \right)^{1/2} \approx 310\ \mu\mathrm{m}. \tag{58}$$

The average diameter of the circumscribed spheres

$$\delta_u \approx 380\ \mu\mathrm{m} \tag{59}$$

is an upper bound.

Figure 13 shows various estimates of differential permeabilities. The four solid curves representing differential permeabilities are obtained from estimating the velocity integral as

$$|\mathbf{w}(\mathbb{W}_x(\ell))| \approx V(\mathbb{W}_x(\ell)) k_{i\,x}(\phi,\sigma) \tag{60}$$

with expressions for $k_x(\phi,\sigma)$ taken from Eqs. (52)–(56) with $i = \mathrm{BZ,ZP,KC,MN}$ and parameters $\delta_0 = 250\ \mu\mathrm{m}$, $\delta = \delta_v \approx 295\ \mu\mathrm{m}$, and $G = 3$, $\mathcal{T} = 2.5$, and $\phi_p = 0.02$. The subscript x signifies that the region of integration changes along the x directions. The resulting estimates for the differential permeability are then

$$\kappa_{i\,x}(V_x) = k_{i\,x}(\psi_x(V_x), \tau_x(V_x)), \tag{61}$$

where $i = \mathrm{BZ}$ (red curve), $i = \mathrm{ZP}$ (green curve), $i = \mathrm{KC}$ (black curve), $i = \mathrm{MN}$ (blue curve), and $V_x = V(\mathbb{W}_x(\ell))$. The estimates for $i = \mathrm{KC}$ (black curve) and $i = \mathrm{MN}$ (blue curve) are expected to be systematically too high, because the Carman-Kozeny expression for granular media is based on nonoverlapping grains.

The symbols in Fig. 13 are the permeabilities obtained by numerical solution of Eq. (1) for the discretized sample a8*.gbd.gz from [40]. Figure 13 shows approximate numerical results for permeabilities $\widetilde{k}_{xx}$ (crosses) and differential permeabilities $\widetilde{\kappa}_{xx}$ (stars) with $\mathbb{W}(\ell) = \mathbb{W}_x(\ell)$ from Eq. (36a) computed from the discretization of the continuum sample. Their numerical values are given in Table I. These computations represent the first measurement of differential permeabilities to our knowledge. The indices xx indicate that inlet and outlet and $\partial\mathbb{S}_\mathrm{i}$,$\partial\mathbb{S}_\mathrm{o}$ are the faces perpendicular to the x direction. On the right the results for $\widetilde{k}_{yy}(\mathbb{P})$ (triangle) and $\widetilde{k}_{zz}(\mathbb{P})$ (circle) for the full sample are also shown. The numerical values for permeabilities $\widetilde{k}$ (crosses) and differential permeabilities $\widetilde{\kappa}$ (stars) all seem to fall between the curves of the empirical correlations.

TABLE I. Overview of the computed permeabilities $\widetilde{k}_{xx}$ and differential permeabilities $\widetilde{\kappa}_{xx}$ of the discretized sample a8*.gbd.gz from [40] with a resolution of $8 \times 15\,000/16\,384 = 7.3242\ \mu$m for measurement cells $\mathbb{W}_x(\ell) = \mathbb{W}(\ell,L,L)$ with different ℓ. Total wall time was around 84 h.

ℓ (mm)	V_x (mm^3)	$\widetilde{k}_{xx}$ (mD)	$\widetilde{\kappa}_{xx}$ (mD)	CPUs	Wall time
3.311	745	1062	1007	512	1.9 h
3.618	814	1060	917	512	2.4 h
4.197	944	1055	981	512	3.2 h
4.636	1043	1046	1013	512	3.8 h
5.310	1195	1047	1027	512	5.0 h
7.859	1768	1024	840	512	10.6 h
10.386	2338	1018	887	512	16.5 h
11.792	2655	1016	982	512	21.7 h
15.0	3375	1008	—	1024	18.6 h

The numerical solution of Eq. (1) for the full sample leads to a system of equations with roughly 5×10^9 unknowns whose solution requires substantial computational facilities and resources. To the best of our knowledge numerical solutions for systems of size $2048 \times 2048 \times 2048$ are worldwide among the largest computational efforts of precision permeametry at present. All computations were performed on the recently installed Cray XC30 (Hornet) and the earlier Cray XE6 (Hermit) machines at HLRS Stuttgart using the massively parallel algorithm developed in [47]. For some details concerning algorithms and methods used to solve Eq. (1), see Appendix C. The numerical results are summarized in Table I together with the numerical resources (number of CPUs and wall time) required for their calculation.

Table I seems to suggest that the conventional permeabilities $\widetilde{k}_{xx}(V_x)$ are systematically larger than the newly introduced differential permeabilities. The numerical results suggest

$$\begin{aligned} \widetilde{k}_{xx}(V_x) > \widetilde{\kappa}_{xx}(V_x) &= \frac{d[V_x \widetilde{k}_{xx}(V_x)]}{dV_x} \\ &= \widetilde{k}_{xx}(V_x) + \widetilde{k}'_{xx}(V_x) \end{aligned} \tag{62}$$

and hence the derivative $\widetilde{k}'_{xx}(V_x) < 0$ is negative. Indeed $\widetilde{k}_{xx}(V_x)$ is seen to decrease nearly monotonically with an average slope of $-0.020\,53$ mD/mm^3 (computed from the first and last data points). This differs from the case of differential porosities and surface densities seen in Figs. 7 and 8 where the differential quantities fluctuate around the nondifferential ones. Conventional and differential permeabilities must approach each other for a homogeneous medium. The nearly monotonic decrease of $\widetilde{k}(V_x)$ suggests that the asymptotic regime has not been reached. Linear extrapolation with the slope $-0.020\,53$ mD/mm^3 to a value of 950 mD would suggest

that the asymptotic regime is reached around 4000 mm^3. We attribute the fact that $\widetilde{\kappa}_{xx}(V_x)$ does not fluctuate around $\widetilde{k}_{xx}(V_x)$ to the nonadditivity of permeability, contrary to the additivity of porosity or other Minkowski functionals (see [5,37]).

The differential permeabilities $\widetilde{\kappa}(V_x)$ are seen to fluctuate. The fluctuations appear to be correlated with the fluctuations of differential porosity and differential surface density although more computations would be needed to ascertain the truth of this observation. However, the apparent correlations suggest that differential permeabilities can be used to characterize heterogeneities in transport properties in the same way as differential porosities (and differential surface densities) can be used to characterize heterogeneities in geometric properties.

VII. CONCLUSION

Differential permeametry and porosimetry were introduced as precision tools into the analysis and modeling of porous media. The methods are exemplified using a very homogeneous, carefully calibrated continuum model for Fontainebleau sandstone. The Fontainebleau sample is publicly available on the worldwide web as a benchmark for methodical studies of correlated random media.

High-precision porosimetry yields porosity and internal surface area densities of the continuum model with floating point accuracy. Continuum results with floating point precision have been compared quantitatively to discrete approximations obtained from synthetic microcomputed tomography, while previous measurements using approximate synthetic microcomputed tomography were based on extrapolation of resolution-dependent measurements. Differential porosities and differential surface area densities allow geometrical fluctuations to be distinguished from discretization effects and numerical noise. In the present study the analysis shows unambiguously that despite the homogeneous visual appearance spatial self-averaging is insufficient due to geometric fluctuations. In this way high-precision porosimetry can help to sharpen the pervasive REV concept.

Differential porosimetry and Fourier analysis reveal subtle periodic correlations. The findings uncover small oscillatory correlations with a period of roughly 850 μm, thus implying that the sample is not strictly stationary. The correlations are attributed to the deposition algorithm that was used to ensure the grain overlap constraint. Differential permeabilities are introduced and computed numerically from discretized approximations to the continuum model structure. Differential porosities and permeabilities provide detailed and quantitative information about geometrical fluctuations and their quantitative importance for flow and transport.

ACKNOWLEDGMENTS

The authors are very grateful to Jens Harting and Martin Hecht for computational resources and support. This work has been supported by the Deutsche Forschungsgemeinschaft (SFB 716).

APPENDIX A

The transformation of an axis-angle rotation $\mathbf{a} = |\mathbf{a}|\mathbf{e} \in \mathbb{B}_{\mathbf{0},2\pi}$ from the model description to a rotation matrix $\mathsf{B} = (\mathsf{b}_{ij})$ reads

$$\mathsf{b}_{11} = e_x^2(1-\cos|\mathbf{a}|)+\cos|\mathbf{a}|, \tag{A1a}$$
$$\mathsf{b}_{12} = e_x e_y(1-\cos|\mathbf{a}|)-e_z\sin|\mathbf{a}|, \tag{A1b}$$
$$\mathsf{b}_{13} = e_x a_z(1-\cos|\mathbf{a}|)+e_y\sin|\mathbf{a}|, \tag{A1c}$$
$$\mathsf{b}_{21} = e_x e_y(1-\cos|\mathbf{a}|)+e_z\sin|\mathbf{a}|, \tag{A1d}$$
$$\mathsf{b}_{22} = e_y^2(1-\cos|\mathbf{a}|)+\cos|\mathbf{a}|, \tag{A1e}$$
$$\mathsf{b}_{23} = e_y e_z(1-\cos|\mathbf{a}|)-e_x\sin|\mathbf{a}|, \tag{A1f}$$
$$\mathsf{b}_{31} = e_x e_z(1-\cos|\mathbf{a}|)-e_y\sin|\mathbf{a}|, \tag{A1g}$$
$$\mathsf{b}_{32} = e_y e_z(1-\cos|\mathbf{a}|)+e_x\sin|\mathbf{a}|, \tag{A1h}$$
$$\mathsf{b}_{33} = e_z^2(1-\cos|\mathbf{a}|)+\cos|\mathbf{a}|. \tag{A1i}$$

In previous publications [6–8,21] the orientation was often specified as a unit quaternion $\mathbf{q}$. The transformation from a quaternion $\mathbf{q} = (q_x,q_y,q_z,q_w)$ to a rotation matrix $\mathsf{B} = (\mathsf{b}_{ij})$ reads

$$\mathsf{b}_{11} = 1-2\left(q_y^2+q_z^2\right), \tag{A2a}$$
$$\mathsf{b}_{12} = 2(q_x q_y+q_w q_z), \tag{A2b}$$
$$\mathsf{b}_{13} = 2(q_x q_z-q_w q_y), \tag{A2c}$$
$$\mathsf{b}_{21} = 2(q_x q_y-q_w q_z), \tag{A2d}$$
$$\mathsf{b}_{22} = 1-2\left(q_x^2+q_z^2\right), \tag{A2e}$$
$$\mathsf{b}_{23} = 2(q_y q_z+q_w q_x), \tag{A2f}$$
$$\mathsf{b}_{31} = 2(q_x q_z+q_w q_y), \tag{A2g}$$
$$\mathsf{b}_{32} = 2(q_y q_z-q_w q_x), \tag{A2h}$$
$$\mathsf{b}_{33} = 1-2\left(q_x^2+q_y^2\right). \tag{A2i}$$

In [21], the orientation was given as three Tait-Bryan rotation angles $\theta_1,\theta_2,\theta_3$. The transformation from Tait-Bryan angles $\theta_1,\theta_2,\theta_3$ to a unit quaternion $\mathbf{q} = (q_x,q_y,q_z,q_w)$ reads

$$q_x = -\sin\frac{\theta_1}{2}\cos\frac{\theta_2}{2}\cos\frac{\theta_3}{2}+\cos\frac{\theta_1}{2}\sin\frac{\theta_2}{2}\sin\frac{\theta_3}{2}, \tag{A3a}$$
$$q_y = -\cos\frac{\theta_1}{2}\sin\frac{\theta_2}{2}\cos\frac{\theta_3}{2}-\sin\frac{\theta_1}{2}\cos\frac{\theta_2}{2}\sin\frac{\theta_3}{2}, \tag{A3b}$$
$$q_z = -\cos\frac{\theta_1}{2}\cos\frac{\theta_2}{2}\sin\frac{\theta_3}{2}+\sin\frac{\theta_1}{2}\sin\frac{\theta_2}{2}\cos\frac{\theta_3}{2}, \tag{A3c}$$
$$q_w = +\cos\frac{\theta_1}{2}\cos\frac{\theta_2}{2}\cos\frac{\theta_3}{2}+\sin\frac{\theta_1}{2}\sin\frac{\theta_2}{2}\sin\frac{\theta_3}{2}. \tag{A3d}$$

APPENDIX B

Generally, a polyhedron $\mathbb{G} \subset \mathbb{R}^3$ is specified as an intersection of m closed half spaces

$$\mathbb{G} = \bigcap_{j=1}^{m} \mathbb{H}_j \tag{B1}$$

with

$$\mathbb{H}_j = \{\mathbf{x} \in \mathbb{R}^3 : (\mathbf{x}-\mathbf{x}_j)\cdot\mathbf{n}_j \leqslant 0\}, \tag{B2}$$

where $\mathbf{x}_j$ is a point on the bounding plane $\partial\mathbb{H}_j$ and $\mathbf{n}_j$ is a face normal pointing to the outside of $\mathbb{G}$.

In the Fontainebleau model all grains have $m = 18$. Each grain $\mathbb{G}$ in the Fontainebleau model is a convex and bounded polyhedron [of type T, located at position $\mathbf{r}$, scaled by a factor R and oriented by a vector $\mathbf{a}$ (rotation matrix B)]. It is obtained

as $\mathbb{G} = R\mathsf{B}\mathbb{G}^0 + \mathbf{r}$ by translation, rotation, and rescaling of a grain template $\mathbb{G}^0$ in normal position. A grain template $\mathbb{G}^0 = \bigcap_{j=1}^m \mathbb{H}_j^0$ in its normal position, size, and orientation is defined by m half spaces $\mathbb{H}_j^0, j = 1,\ldots,m$, each defined by a vector $\mathbf{x}_j^0$ such that

$$\mathbb{H}_j^0 = \left\{\mathbf{x} \in \mathbb{R}^3 : \left(\mathbf{x} - \mathbf{x}_j^0\right) \cdot \mathbf{x}_j^0 \leqslant 0\right\} \tag{B3}$$

holds. The vectors $\mathbf{x}_j^0$ are simultaneously face normals and points on the face itself. After rotating the grain by matrix B, scaling by scalar R, and translating by vector $\mathbf{r}$, the parameters $\mathbf{n}_j$ and $\mathbf{x}_j$ in Eq. (B2) read

$$\mathbf{n}_j = \mathsf{B}\mathbf{x}_j^0, \tag{B4a}$$

$$\mathbf{x}_j = \left(R\mathsf{B}\mathbf{x}_j^0 + \mathbf{r}\right), \tag{B4b}$$

with $\mathbf{x}_j^0$ being the template parameters from Eq. (B3).

Picking (without loss of generality) any of the vertices of the grain $\mathbb{G}$ the numbering of the m bounding planes $\partial\mathbb{H}_j$, $j = 1,\ldots,m$ can always be chosen such that the first three of them intersect in the chosen vertex of $\mathbb{G}$. Denoting this vertex as $\mathbf{s}_1$, it follows that the intersection

$$\{\mathbf{s}_1\} = \partial\mathbb{H}_1 \cap \partial\mathbb{H}_2 \cap \partial\mathbb{H}_3 \subset \mathbb{G} \tag{B5}$$

is a single point. The volume V of $\mathbb{G}$ is then given by

$$V = \frac{1}{3}\sum_{j=1}^{m} A_j(\mathbf{x}_j - \mathbf{s}_1)\cdot\mathbf{n}_j, \tag{B6}$$

where A_j is the area of the polygon $F_j = \partial\mathbb{H}_j \cap \mathbb{G}$. From $\mathbf{s}_1 \in \partial\mathbb{H}_1$, $\mathbf{s}_1 \in \partial\mathbb{H}_2$, and $\mathbf{s}_1 \in \partial\mathbb{H}_3$ follows $(\mathbf{x}_j - \mathbf{s}_1)\cdot\mathbf{n}_j = 0$ for $j = 1,2,3$. Therefore, the first three terms in the summation in Eq. (B6) vanish and the summation

$$V = \frac{1}{3}\sum_{j=4}^{m} A_j(\mathbf{x}_j - \mathbf{s}_1)\cdot\mathbf{n}_j \tag{B7}$$

starts from $j = 4$. It remains to determine the areas A_j.

The area A of a plane, convex polygon $F \subset \mathbb{R}^3$ defined by its vertices $\mathbf{c}_k \in \mathbb{R}^3$, $k = 1,\ldots,q$ can be efficiently calculated by projecting the vertices onto one of the coordinate planes as long as the area of the projected polygon does not vanish. For reasons of numerical accuracy the coordinate plane should be chosen such that the surface area of the projected polygon is maximal. This is the coordinate plane which is perpendicular to the largest component of the normal vector of the polygon F.

Let $\mathbf{n} = (n_x,n_y,n_z)$ be the normal vector of the polygon F. Then its vertices $\mathbf{c}_k = (c_{kx},c_{ky},c_{kz})$ are projected onto the vertices $\mathbf{c}_k^x,\mathbf{c}_k^y$ or $\mathbf{c}_k^z \in \mathbb{R}^2$ according to the following rules:

(a) Case 1: (Projection along x onto yz plane)
If $|n_x| \geqslant |n_y|$ and $|n_x| \geqslant |n_z|$, then $\mathbf{c}_k^x = (c_{ky},c_{kz})$.

(b) Case 2: (Projection along y onto xz plane)
If $|n_y| > |n_x|$ and $|n_y| \geqslant |n_z|$, then $\mathbf{c}_k^y = (c_{kz},c_{kx})$.

(c) Case 3: (Projection along z onto xy plane)
If $|n_z| > |n_x|$ and $|n_z| > |n_y|$, then $\mathbf{c}_k^z = (c_{kx},c_{ky})$.

(The different choice of $>$ or $\geqslant$ in these cases serves to cover also those situations in which equalities among $|n_x|,|n_y|,|n_z|$ occur.) As a result the projected polygon is defined by its vertices $\mathbf{c}_k^\alpha, k = 1,\ldots,q$ where $\alpha = x$ (Case 1), $\alpha = y$ (Case 2), or $\alpha = z$ (Case 3). In the following the index α refers to a single one of the three cases. Subsequently the projected vertices $\mathbf{c}_k^\alpha$ are translated by the vector $-\mathbf{c}_1^\alpha$,

$$\mathbf{c}_k^\alpha = \mathbf{c}_k^\alpha - \mathbf{c}_1^\alpha, \quad k = 1,\ldots,q, \tag{B8}$$

and renumbered such that the sequence of unit vectors $\mathbf{c}_k^\alpha/|\mathbf{c}_k^\alpha|, k = 2,\ldots,q$, describes a counterclockwise rotation. This is achieved computationally by permuting the indices until for all $k \in \{2,\ldots,q-1\}$

$$\mathbf{c}_k^\alpha \times \mathbf{c}_{k+1}^\alpha \geqslant 0 \tag{B9}$$

holds, where $\mathbf{a}\times\mathbf{b} = a_xb_y - a_yb_x$ is the two-dimensional cross product. The area of the projected polygon is then given by

$$A_\perp^\alpha = \frac{1}{2}\sum_{k=2}^{q-1} \mathbf{c}_k^\alpha \times \mathbf{c}_{k+1}^\alpha, \tag{B10}$$

where α corresponds to one of the three cases. Finally, the area of the original (not projected) polygon is

$$A = \frac{A_\perp^\alpha}{|n_\alpha|}, \tag{B11}$$

where α, as before, indicates which one of the three possible projections was applied.

APPENDIX C

The Stokes problem (1) is solved using a modified and parallelized version of the well-known SIMPLE algorithm on a staggered grid [47,48]. The SIMPLE algorithm is matrix-free and has minimal memory requirements. It is parallelizable and performs well for porous media. The iterative algorithm uses a pressure correction method for solving the (dimensionless) time-dependent Stokes equation

$$\frac{\partial\mathbf{v}(\mathbf{x},t)}{\partial t} = -\nabla p(\mathbf{x},t) + \Delta\mathbf{v}(\mathbf{x},t), \tag{C1a}$$

$$\nabla\cdot\mathbf{v}(\mathbf{x},t) = 0, \tag{C1b}$$

in $\mathbb{P}$ for the pressure $p(\mathbf{x},t)$ and the velocity $\mathbf{v}(\mathbf{x},t)$. In the limit of large times, the time evolution of the solution $p(\mathbf{x},t)$, $\mathbf{v}(\mathbf{x},t)$ converges towards the stationary solution $p(\mathbf{x})$, $\mathbf{v}(\mathbf{x})$. (The use of all symbols of the notation is restricted to this Appendix to avoid any conflict with the rest of the text.)

The algorithm consists of the following schematic steps:

(1) Initially at step $n = 0$, the initial pressure and velocity fields are specified from prior knowledge, expectation, or computation as $p^0(\mathbf{x})$ and $\mathbf{v}^0(\mathbf{x})$.

(2) Given the velocity $\mathbf{v}^n$ and pressure p^n at step n, an intermediate velocity $\mathbf{v}^*$ is calculated according to

$$\mathbf{v}^* = \mathbf{v}^n + \delta t\cdot(-\nabla p^n + \Delta\mathbf{v}^n) \tag{C2}$$

for a sufficiently small time interval δt.

(3) Given $\mathbf{v}^*$, the pressure-correction equation for the correction field p'

$$\Delta p' = \frac{1}{\delta t}\nabla\cdot\mathbf{v}^* \tag{C3}$$

is solved.

(4) Pressure and velocity are updated to step $n+1$ according to

$$p^{n+1} = p^n + \alpha_p \cdot p', \tag{C4a}$$

$$\mathbf{v}^{n+1} = \mathbf{v}^* - \alpha_v \cdot \delta t \nabla p', \tag{C4b}$$

with underrelaxation factors α_p for pressure and α_v for velocity.

(5) Finally, error estimates for pressure and velocity are computed and the algorithm returns to step C as long as the error is above the desired accuracy, else it stops.

The algorithm is parallelized by identifying and dividing the domain into layers such that each layer can be computed parallel to the rest.

[1] R. Elliott, J. Krumhansl, and P. Leath, Rev. Mod. Phys. **46**, 465 (1974).

[2] R. Landauer, in *Electrical Transport and Optical Properties of Inhomogeneous Materials*, edited by J. Garland and D. Tanner (American Institute of Physics, New York, 1978), p. 2.

[3] S. Havlin and D. Ben-Avraham, Adv. Phys. **36**, 695 (1987).

[4] R. Hilfer, Adv. Chem. Phys. **92**, 299 (1996).

[5] R. Hilfer, Transp. Porous Media **46**, 373 (2002).

[6] B. Biswal, P.-E. Øren, R. J. Held, S. Bakke, and R. Hilfer, Phys. Rev. E **75**, 061303 (2007).

[7] B. Biswal, P. Øren, R. Held, S. Bakke, and R. Hilfer, Image Anal. Stereol. **28**, 23 (2009).

[8] B. Biswal, R. J. Held, V. Khanna, J. Wang, and R. Hilfer, Phys. Rev. E **80**, 041301 (2009).

[9] S. Roth, B. Biswal, G. Afshar, R. Held, P. Øren, L. Berge, and R. Hilfer, AAPG Bull. **95**, 925 (2011).

[10] C. P. Fernandes, F. S. Magnani, P. C. Philippi, and J. F. Daian, Phys. Rev. E **54**, 1734 (1996).

[11] T. Hou and X. Wu, J. Comput. Phys. **134**, 169 (1997).

[12] T. Hughes, G. Feijoo, L. Mazzei, and J. Quincy, Comput. Methods Appl. Mech. Eng. **166**, 3 (1998).

[13] Y. Efendiev, T. Hou, and X. Wu, SIAM J. Numer. Anal. **37**, 888 (2000).

[14] T. Arbogast and K. Boyd, SIAM J. Numer. Anal. **44**, 1150 (2006).

[15] J. S. Andrade, Jr., D. A. Street, T. Shinohara, Y. Shibusa, and Y. Arai, Phys. Rev. E **51**, 5725 (1995).

[16] J. R. Banavar and D. L. Johnson, Phys. Rev. B **35**, 7283(R) (1987).

[17] L. Furuberg, K. J. Maloy, and J. Feder, Phys. Rev. E **53**, 966 (1996).

[18] C. Manwart and R. Hilfer, Phys. Rev. E **59**, 5596 (1999).

[19] C. Manwart, S. Torquato, and R. Hilfer, Phys. Rev. E **62**, 893 (2000).

[20] R. Hilfer and C. Manwart, Phys. Rev. E **64**, 021304 (2001).

[21] F. Latief, B. Biswal, U. Fauzi, and R. Hilfer, Physica A **389**, 1607 (2010).

[22] R. Hilfer and T. Zauner, Phys. Rev. E **84**, 062301 (2011).

[23] J. Fredrich, K. Greaves, and J. Martin, Int. J. Rock Mech. Min. Sci. Geomech. Abstr. **30**, 691 (1993).

[24] D. Coker, S. Torquato, and J. Dunsmuir, J. Geophys. Res. **101**, 17497 (1996).

[25] B. Biswal, C. Manwart, R. Hilfer, S. Bakke, and P. Øren, Physica A **273**, 452 (1999).

[26] J.-F. Thovert, F. Yousefian, P. Spanne, C. G. Jacquin, and P. M. Adler, Phys. Rev. E **63**, 061307 (2001).

[27] A. El Bied, J. Sulem, and F. Martineau, Rock Mech. Mining Sci. **39**, 917 (2002).

[28] B. Zinszner and F. Pellerin, *A Geoscientist's Guide to Petrophysics* (Editions Technip, Paris, 2007).

[29] P. Carman, *Flow of Gases Through Porous Media* (Butterworth, London, 1956).

[30] M. Beran, *Statistical Continuum Theories* (Wiley, New York, 1968).

[31] A. Scheidegger, *The Physics of Flow Through Porous Media* (University of Toronto Press, Toronto, 1974).

[32] R. Hilfer, Phys. Rev. B **45**, 7115 (1992).

[33] R. Schneider and W. Weil, *Stochastische Geometrie* (Teubner, Stuttgart, 2000).

[34] H. Federer, *Geometric Measure Theory* (Springer, Berlin, 1969).

[35] M. Berg, O. Cheong, M. Kreveld, and M. Overmars, *Computational Geometry* (Springer, Berlin, 1998).

[36] A. Straub, Analyse poröser Medien auf Basis von Kristalliten, Magisterarbeit, VISUS 2013.

[37] R. Hilfer, in *Räumliche Statistik und Statistische Physik*, edited by D. Stoyan and K. Mecke, Lecture Notes in Physics Vol. 554 (Springer, Berlin, 2000), p. 203.

[38] G. Ziegler, *Lectures on Polytopes* (Springer, Berlin, 1995).

[39] W. Gray, A. Leijnse, R. Kolar, and C. Blain, *Mathematical Tools for Changing Spatial Scales in the Analysis of Physical Systems* (CRC Press, Boca Raton, FL, 1993).

[40] R. Hilfer and T. Zauner, Three-dimensional $(1.5\,\mathrm{cm})^3$ microstructures at submicron resolution, 2011, available from http://www.icp.unistuttgart.de/microct/.

[41] C. Lang, J. Ohser, and R. Hilfer, J. Microsc. **203**, 303 (2001).

[42] D. Stoyan, W. Kendall, and J. Mecke, *Stochastic Geometry and Its Applications* (Akademie-Verlag/Wiley, Berlin/Chichester, 1987).

[43] A. Lemmer, Porenskalenmodellierung poröser Medien, Ph.D. thesis, Universität Stuttgart, 2015.

[44] P. Doyen, J. Geophys. Res. **93**, 7729 (1988).

[45] G. Mavko and A. Nur, Geophysics **62**, 1480 (1997).

[46] T. Bourbie and B. Zinszner, J. Geophys. Res. **90**, 11524 (1985).

[47] A. Lemmer and R. Hilfer, J. Comput. Phys. **281**, 970 (2015).

[48] S. Patankar and D. Spalding, Int. J. Heat Mass Transfer **15**, 1787 (1972).